

Spectrally encoded extended source optical coherence tomography

Xinyu Liu,¹ Xiaojun Yu,¹ Hongying Tang,¹ Dongyao Cui,¹ Meghna R. Beotra,² Michael J. A. Girard,^{2,3} Ding Sun,¹ Jun Gu,¹ and Linbo Liu^{1,4,*}

¹School of Electrical and Electronic Engineering, Nanyang Technological University, Singapore 639798, Singapore

²Department of Biomedical Engineering, National University of Singapore, Singapore 117575, Singapore

³Singapore Eye Research Institute, Singapore National Eye Centre, Singapore 168751, Singapore

⁴School of Chemical and Biomedical Engineering, Nanyang Technological University, Singapore 637459, Singapore

*Corresponding author: liulinbo@ntu.edu.sg

Received September 15, 2014; accepted October 20, 2014;

posted November 4, 2014 (Doc. ID 222884); published December 5, 2014

We have developed an extended source optical coherence tomography (SEES-OCT) technique in an attempt to improve signal strength for ophthalmic imaging. A line illumination with a visual angle of 7.9 mrad is produced by introducing a dispersive element in the infinity space of the sample arm. The maximum permissible exposure (MPE) of such an extended source is 3.1 times larger than that of a “standard” point source OCT, which corresponds to sensitivity improvement of 5 dB. The advantage of SEES-OCT in providing superior penetration depth over a point source system is demonstrated using swine eye tissues *ex vivo*. © 2014 Optical Society of America

OCIS codes: (170.4500) Optical coherence tomography; (170.3880) Medical and biological imaging.

<http://dx.doi.org/10.1364/OL.39.006803>

Optical coherence tomography (OCT) has been established as an imaging tool for diagnosis of various eye diseases. Current Fourier domain OCT, including spectral domain OCT and swept source OCT, is capable of performing three-dimensional (3D) imaging of human eyes *in vivo* and visualizing many tissue structures in the posterior segment [1–3]. However, there are two unmet clinical needs: visualizing deep tissue structures [4–6] and faster scanning to reduce motion artifacts in 3D images [7,8], both of which require better sensitivity. The sensitivity of an existing ophthalmic OCT system is mainly limited by the maximum permissible radiant exposure imposed by the laser safety standards [9]. OCT devices operating with an extended source [10,11] can potentially improve imaging sensitivity because higher MPE is allowed for an extended source than that of a point source [9]. Therefore, an extended source OCT technology will effectively enhance the sensitivity thereby increasing the penetration depth.

In this report, we report a spectrally encoded extended source OCT (SEES-OCT) technique that allows significantly higher MPE than that provided by commercial ophthalmic OCT systems. To the best of our knowledge, this has never been reported before. Imaging was performed using optic nerve head (ONH) tissues from enucleated swine eyes to demonstrate a sensitivity advantage of 5 dB over the corresponding point source system without significant degradation in transverse resolution. The hardware system of SEES-OCT device is almost the same as the current point source system except for one additional element in the infinity space. Therefore, any existing ophthalmic OCT system can be easily modified so that it can be switched between the point source mode and the extended source mode. Based on its merits in sensitivity and flexibility, this technique may help visualize deep ocular tissue structures that are at risk of damage in glaucoma such as the lamina cribrosa, the posterior sclera, and the retro-laminar tissues [4,6,12].

The SEES-OCT setup assumes a free-space Michelson interferometer design (Fig. 1). The output of a superluminescent diode (SLD) array (Exalos Ultra-Broadband EBS4C32) is collimated by lens L1 (AC050-010-B, $f = 10$ mm, Thorlabs Inc.) with optical power of 5.72 mW over a 3-dB spectral range of 950–1130 nm. A 50:50 non-polarizing beam splitter (BS) splits the source beam into a reference beam and a sample beam. An equilateral prism (#43-494, N-SF18, Edmund Optics) transforms the collimated sample beam into a fan beam by separating radiation of different wavelength over a propagation angular range of 7.9 mrad (full angle at half-maximum). By use of an objective lens of 50-mm focal length (AC254-050-B, Thorlabs Inc.), the full length at half-maximum of the illumination line on the sample is ~ 380 μm . Light backreflected from the reference arm and backscattered from the sample arm is recombined through the beam splitter before directed to a spatial filter consisting of

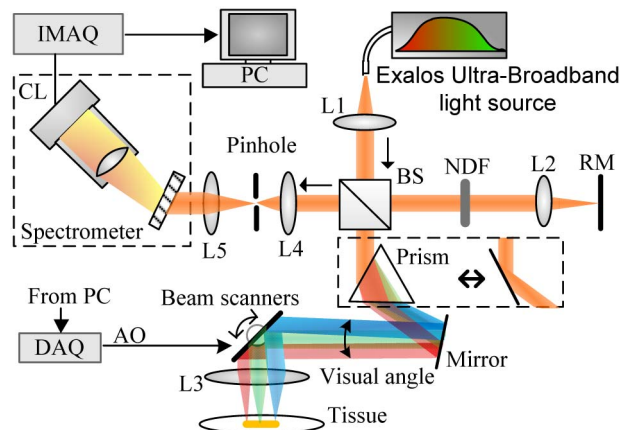


Fig. 1. Schematic of SEES-OCT system. AO, analog output; BS, nonpolarizing beam splitter; IMAQ, image acquisition board; L1-5, achromatic lenses; DAQ, data acquisition card; NDF, neutral density filter; PC, personal computer; CL, camera link cable; RM, reference mirror.

a focusing lens L4 (AC050-010-B, $f = 10$ mm, Thorlabs Inc.), a 10- μm pinhole, and another collimation lens L5 (AC127-030-B, $f = 30$ mm, Thorlabs Inc.). The spectrometer is composed of an 1450 lines/mm volume phase holographic transmission grating (1030 nm, Wasatch Photonics Inc.), a camera lens (Nikon AF Nikkor 50 mm $f/1.8D$), and a linear camera (Sensors Unlimited GL2048 L). We used 2048 camera pixels to detect a total spectral range from 925 to 1150 nm and each camera pixel corresponds to a spectral band of ~ 0.11 nm. We digitized the detected signal at 12-bit resolution and transferred it to the personal computer through the camera link cables and an image acquisition board (KBN-PCE-CL4-F, Bitflow). The camera and the galvo scanners are synchronized by a triggering signal generated by the computer. It is worth mentioning that by replacing the prism with a mirror, a SEES-OCT device can be changed to a "standard" point source OCT device (Fig. 1, dashed box).

The illumination line is aligned in the same direction as the fast scanning direction of the galvo scanners, so that at a given sample point O the wavelength sweeps over time as the fast scanning mirror scans the sample beam across it [Fig. 2(a)]. As a result, at the point O , the arrival time (A-line sequence number) of different spectral bands is dependent on the refractive index of the prism and the galvo scanning speed. Fig. 2(b) shows a B-scan frame consisting of 512 consecutive spectral lines acquired when the fast scanning mirror scans the sample beam across a chromium-coated pattern of a United States Air Force (USAF) 1951 resolution target with the reference path blocked. Then the B-scan frame was remapped by arrival time so that every vertical spectral line contained the spectrum from only one sample point [Fig. 2(b')]. Specifically, an edge curve of the coated pattern [green arrow in Fig. 2(b)] was used to extract the delay time n (in A-line cycle) of different spectral bands arriving at the same point with regard to the first spectral band. The edge curve was extracted using image processing method. Note that the edge curve was actually the spectrum from one single point on the sample. After the arrival-time remapping, the points on the curve should be in the same A-line, corresponding

to a straight vertical line in the B-scan frame. Therefore, the A-line number difference between m th camera pixel and the 1st pixel on this curve was the time delay n of the spectral band detected by the camera pixel m . This discrete time delay data was further processed using 6th-order polynomial fitting to obtain a continuous curve [Fig. 2(c)], which was used as a lookup table to remap spectral data. The B-scan range was 4.37 mm so that the spectral remapping process results in a scan margin of 50 A-lines [yellow arrow, Fig. 2(b')] where axial resolution is degraded.

To test whether the transverse resolution of SEES-OCT may be degraded with respect to the corresponding point source OCT system, we scanned the resolution target using the SEES-OCT system. We predicted the transverse focal spot of the point source system to be 21 μm ($1/e^2$ power level) based on the mode field diameter of the input single mode fiber (4.2 μm at 980 nm, Corning HI 980) and the magnification of the sample arm optics (0.2 \times). In Fig. 3(a), the vertical direction is the direction of the illumination line. Therefore, the vertical line patterns reflect the resolving power of SEES-OCT, while the horizontal line patterns reflect that of the corresponding point source OCT. We observed slight degradation in transverse resolving power in the vertical direction with regard to the diffraction-limited resolution in the horizontal direction. The chromium patterns of element 6 in group 4 [Fig. 3(a), arrow] with a line spacing of 17.5 μm can be clearly resolved [Fig. 3(a), inset]. To characterize the axial resolution of the system, we investigated the axial point spread functions (PSF) by measuring the A-line profiles of a partially reflecting mirror sample using both SEES-OCT and the point source OCT. The axial resolution of SEES-OCT was tested to be 4.6 μm in air [Fig. 3(b)], which is 10% lower than that of the point source system. This may be because in SEES-OCT, the effective spectral bandwidth of the sample field reflected from a specular object is smaller than that of the point source case. Since different spectral bands are reflected at different locations of the galvo mirror, at a given sample point, the incident angles of different spectral bands are slightly different. Therefore, when the spectral bands are

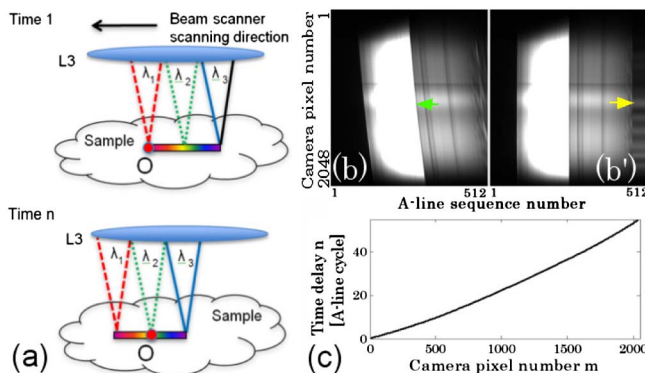


Fig. 2. (a) Schematic of wavelength sweeping. L3, objective lens; black arrow, direction of the fast scan. (b) 512 consecutive spectra acquired when scanning across a pattern of the resolution target. Green arrow, edge line; (b') spectra in (b) after remapping. Yellow arrow, scan margin. (c) Time delay of different spectral bands.

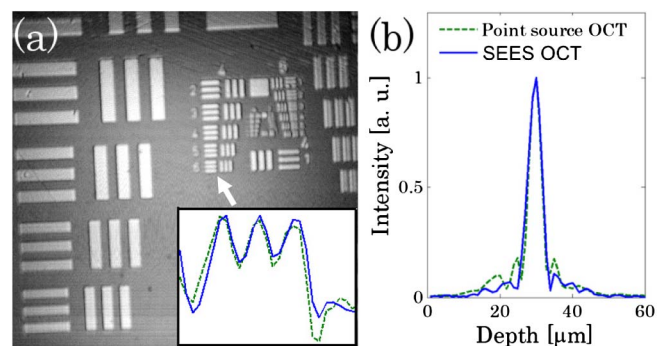


Fig. 3. Spatial resolution: SEES-OCT versus point source OCT. (a) An *en face* view of a 3D image of USAF 1951 resolution target acquired using SEES-OCT. Inset: cross-sections of group 4, element 6 in horizontal (blue solid curve), and vertical (green dashed curve) directions. (b) Axial point-spread function of SEES-OCT (blue solid curve) compared with that of the point source OCT (green dashed curve).

reflected by the specular sample, the detection efficiency drops slightly for the spectral bands at both ends of the spectral range where the reflection angles are suboptimal for coupling into the pinhole. However, such a problem will be minimized for backscattered signal.

The MPE at the cornea for an extended source is obtained by multiplying the MPE of a point source by a parameter C_E , which is the arithmetic mean of the minimum visual angle α_{\min} (1.5 mrad) and the visual angle α (Fig. 1) [9]: $C_E = (\alpha + \alpha_{\min})/2/\alpha_{\min} = 3.135$. This MPE advantage of SEES-OCT over point source OCT provides a sensitivity gain of 5 dB given the fact that the noise of both systems is the same. Assuming the maximum input power at the cornea limited by the MPE of the point source OCT is 0.67 mW, the corresponding maximum permissible optical power for the SEES-OCT is 2.1 mW. To characterize the sensitivity of the SEES-OCT system, we measured the signal-to-noise ratio (SNR) using a partially reflecting mirror sample (-46.4 dB reflectivity) when the pathlength difference between the mirror sample and reference arm was maintained at 0.3 mm. The sensitivity was measured to be 102.2 dB. In order to understand the measured sensitivity, we analyzed the SNR using the following formulas [13]:

$$S[\text{dB}] = 10 \times \log\left(\frac{N_{\text{ref}} \times \sum N_S}{N_{\text{sh}}^2 + N_{\text{el}}^2 + N_{\text{RIN}}^2}\right) \quad (1)$$

$$N_{\text{RIN}} = (f/\Delta\nu)^{1/2} N_{\text{ref}} \quad (2)$$

$$N_{\text{sh}} = (N_{\text{ref}})^{1/2} \quad (3)$$

where N_{ref} is the number of electrons per pixel generated by the reference arm light, N_{el} is the electrical noise of the photodetector, N_{sh} is the number of shot noise electrons, N_{RIN} is the relative intensity noise, f is the reciprocal of twice the exposure time of the CCD, $\Delta\nu$ denotes the FWHM spectral bandwidth of the reference light received by a single pixel, and $\sum N_S$ denotes the sum of electrons over the entire array generated by the sample arm light returning from a 100% reflector. The full well depth of the camera pixel is $2.1\text{M } e^-$. With a spectrometer efficiency of 0.64 and an average fill factor of 0.7, $N_{\text{ref}} = 937,440e^-$ and $N_{\text{sh}} = 968e^-$. The line rate and the exposure time were 20,000 Hz and 45 μs , respectively. Therefore, the N_{RIN} was calculated to be $665e^-$. The total electrical noise was found to be $872e^-$. $\sum N_S$ was measured to be $5.95 \times 10^{10}e^-$. Using Eq. (1), the sensitivity was estimated to be 104 dB, which was in agreement with our experimental results. The depth performance of SEES-OCT is not significantly different from that of point source OCT, and both have 6 dB of sensitivity roll-off around 1.2 mm [Figs. 4(a) and 4(b)].

In order to demonstrate the potential of SEES-OCT for visualizing tissue structures of the posterior eye segment with enhanced sensitivity, we imaged a swine ONH *ex vivo* using both the SEES-OCT system and the corresponding point source system. Freshly enucleated swine eyes were dissected to expose the ONHs to the focused beam. 3D images were acquired using the SEES-OCT

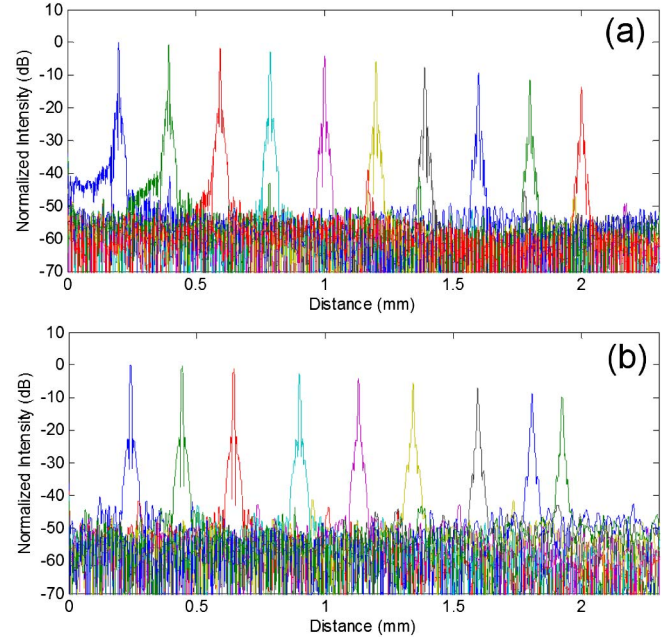


Fig. 4. Axial PSFs for different depth delays: (a) point source OCT system and (b) SEES-OCT system.

system [Figs. 5(a) and 5(a')], and the point source system [Figs. 5(b) and 5(b')] at sample power of 2.1 mW. The image size was 4.37 mm by 4.37 mm by 2.45 mm (x by y by z) with a frame rate of 40 Hz and 512 A-lines per frame. We found that SEES-OCT can image both

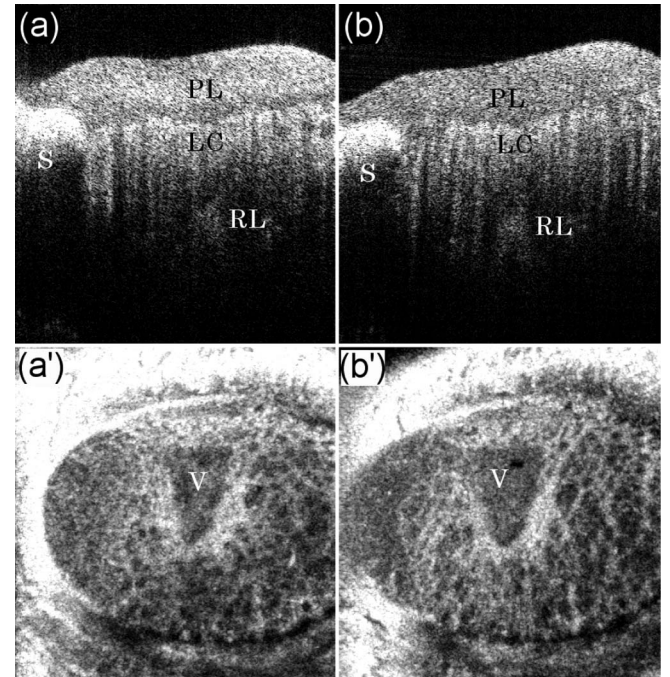


Fig. 5. Cross-sectional (longitudinal) images of a swine ONH tissue acquired using (a) SEES-OCT (2.1 mW sample power) and (b) the point source OCT (2.1 mW sample power), respectively. (a') and (b') Corresponding *en face* images of the lamina cribrosa (LC) region. PL, pre-lamina tissue; S, sclera; RL, retina; V, central retinal vessels.

the lamina cribrosa and the retro-laminar tissues [Fig. 5(a)], and the image quality achieved by the SEES-OCT setup is comparable with that of the point source setup operation at the same sample power [Figs. 5(a) and 5(b)].

SEES-OCT is more sensitive to motion artifacts than its point source counterpart due to effectively prolonged exposure time for a given sample point. Due to this issue, SEES-OCT is better suited as an add-on to point source devices. A simple switch mechanism (Fig. 1, dashed box) will be enough to integrate SEES-OCT in an existing device. By doing this, higher penetration and potentially higher speed can be achieved in the extended source mode without affecting the functions of the point source devices.

In conclusion, we have developed a spectrally encoded extended source OCT technology and demonstrated its potential to image deeper than the existing OCT technology. SEES-OCT can be easily integrated into the existing point source OCT devices as an add-on option with minor hardware changes. Therefore, this technology may help visualize tissue structures that may not be readily seen using a point source system.

We sincerely appreciate funding support from Nanyang Technological University (Startup grant: Linbo Liu), National Research Foundation Singapore (NRF2013NRF-POC001-021), National Medical Research Council Singapore (NMRC/CBRG/0036/2013), and Ministry of Education Singapore (MOE2013-T2-2-107).

References

1. M. Wojtkowski, V. Srinivasan, J. G. Fujimoto, T. Ko, J. S. Schuman, A. Kowalczyk, and J. S. Duker, *Ophthalmology* **112**, 1734 (2005).
2. B. Považay, H. Sattmann, F. Zeiler, J. E. Morgan, C. Falkner-Radler, W. Drexler, C. Glittenberg, B. Hermann, A. Unterhuber, and S. Blinder, *J. Biomed. Opt.* **12**, 041211 (2007).
3. T. Klein, W. Wieser, C. M. Eigenwillig, B. R. Biedermann, and R. Huber, *Opt. Express* **19**, 3044 (2011).
4. T.-W. Kim, L. Kagemann, M. J. Girard, N. G. Strouthidis, K. R. Sung, C. K. Leung, J. S. Schuman, and G. Wollstein, *Curr. Eye Res.* **38**, 903 (2013).
5. S. C. Park, C. G. V. De Moraes, C. C. Teng, C. Tello, J. M. Liebmann, and R. Ritch, *Ophthalmology* **119**, 3 (2012).
6. M. J. A. Girard, N. G. Strouthidis, C. R. Ethier, and J. M. Mari, *Invest. Ophthalmol. Visual Sci.* **52**, 7738 (2011).
7. M. F. Kraus, B. Potsaid, M. A. Mayer, R. Bock, B. Baumann, J. J. Liu, J. Hornegger, and J. G. Fujimoto, *Biomed. Opt. Exp.* **3**, 1182 (2012).
8. J. S. Kim, H. Ishikawa, K. R. Sung, J. Xu, G. Wollstein, R. A. Bilonick, M. L. Gabriele, L. Kagemann, J. S. Duker, and J. G. Fujimoto, *British J. Ophthalmol.* **93**, 1057 (2009).
9. F. C. Delori, R. H. Webb, and D. H. Sliney, *J. Opt. Soc. A* **24**, 1250 (2007).
10. D. J. Fechtig, T. Schmolz, B. Grajciar, W. Drexler, and R. A. Leitgeb, *Opt. Lett.* **39**, 5333 (2014).
11. Y. Nakamura, S. Makita, M. Yamanari, M. Itoh, T. Yatagai, and Y. Yasuno, *Opt. Express* **15**, 7103 (2007).
12. I. A. Sigal, B. Wang, N. G. Strouthidis, T. Akagi, and M. J. Girard, *British J. Ophthalmol.* **98**, ii34 (2014).
13. S. Yun, G. Tearney, B. Bouma, B. Park, and J. de Boer, *Opt. Express* **11**, 3598 (2003).